Interfacial Strain Gradients Control Nanoscale Domain Morphology in Epitaxial BiFeO3 Multiferroic Films

Daniel Sando, Mengjiao Han, Vivasha Govinden, Oliver Paull, Florian Appert, Cécile Carrétéro, Johanna Fischer, Agnès Barthélémy, Manuel Bibes, Vincent Garcia, et al.

Interfacial Strain Gradients Control Nanoscale Domain Morphology in Epitaxial BiFeO₃ Multiferroic Films

Daniel Sando,[1,2,*] Mengjiao Han,[3,4] Vivasha Govinden,[1] Oliver Paull,[1] Florian Appert,[5] Cécile Carrétéro,[6] Johanna Fischer,[6] Agnès Barthélémy,[6] Manuel Bibes,[6] Vincent Garcia,[6] Stéphane Fusil,[6] Brahim Dkhil,[7] Jean Juraszek,[5] Yinlian Zhu,[3] Xiuliang Ma,[3] and Valanoor Nagarajan[1,*]

[1]School of Materials Science and Engineering, UNSW Sydney, High Street, Kensington 2052, Australia
[2]Mark Wainwright Analytical Centre, UNSW Sydney, High Street, Kensington 2052, Australia
[3]Shenyang National Laboratory for Materials Science, Institute of Metal Research, Chinese Academy of Sciences, Wenhua Road 72, 110016 Shenyang, China
[4]University of Chinese Academy of Sciences, Yuquan Road 19, 100049 Beijing, China
[5]Normandie Univ., UNIROUEN, INSA Rouen, CNRS, GPM, 76000 Rouen, France
[6]Unité Mixte de Physique, CNRS, Thales, Univ. Paris-Sud, Palaiseau, France
[7]Laboratoire Structures, Propriétés et Modélisation des Solides, CentraleSupélec, CNRS-UMR8580, Université Paris-Saclay, 91190 Gif-sur-Yvette, France

daniel.sando@unsw.edu.au

nagarajan@unsw.edu.au

Abstract:

Domain switching pathways fundamentally control performance in ferroelectric thin film devices. In epitaxial bismuth ferrite (BiFeO₃) films, the domain morphology is known to influence the multiferroic orders. Whilst both striped and mosaic domains have been observed, the origins of the latter have remained unclear. Here, we show that domain morphology is defined by the strain profile across the film-substrate interface. In samples with mosaic domains, X-ray diffraction analysis reveals strong strain gradients, while geometric phase analysis using scanning transmission electron microscopy finds that within 5 nm of the film-substrate interface, the out-of-plane strain shows an anomalous dip while the in-plane strain is constant. Conversely, if uniform strain is maintained across the interface with zero strain gradient, striped domains are formed. Critically, an *ex-situ* thermal treatment, which eliminates the interfacial strain gradient, converts the domains from mosaic to striped. The antiferromagnetic state of the BiFeO₃ is also influenced by the domain structure, whereby the mosaic domains disrupt the long-range spin cycloid. This work demonstrates that atomic scale tuning of interfacial strain gradients is a powerful route to manipulate the global multiferroic orders in epitaxial films.

Perovskite oxides (with chemical formula ABO_3) are widely studied for their many and varied functional characteristics such as ferroelectricity,[1] magnetism, superconductivity,[2] optical response,[3–6] high dielectric susceptibility and piezoelectricity, colossal magnetoresistance,[7] multiferroism, *etc*. In such materials, the strong correlation between structure and properties underpins their physics and ultimately their functional response.[8–11] The simple perovskite structure can undergo various structural distortions, typically caused either by external hydrostatic pressure or strain. These distortions can be categorized into cation shifts (which for instance can give rise to ferroelectricity)[12] and oxygen octahedron distortions and rotations (which controls the O-B-O bond angle and can for instance influence metal-insulator transitions).[13] The type of distortion present in a given chemical formula is typically dependent on the relative size of the A and B cations.[14]

In traditional ferroelectric perovskites such as $BaTiO_3$ and $PbTiO_3$, a strong dependence of the polar,[9] dielectric, and optical properties[10] has been found, as a function of the imposed strain[9] or hydrostatic pressure.[15] In the case of epitaxial ferroelectric oxide thin films, this strain is typically imposed through an underlying single-crystalline substrate. Termed as strain engineering,[16] the levels of strain achievable can often exceed a few percent, and novel strain-driven functionalities can be realized.[17,18]

Since the properties of a ferroelectric are defined by the mechanical and electrical boundary conditions, playing with the nanoscale strain and/or conductivity properties of the interfacial layers can yield unique and exotic domain structures and changes in functional response.[19,20] For instance, the discovery of nanoscale topological ferroelectric domain arrangements[21–24] can primarily be attributed to this complex interplay between the various interfacial boundary conditions. While the electrical boundary conditions have been widely addressed, strain *gradients* are becoming increasingly important. Indeed, long-range strains, and more specifically strain gradients along with flexoelectricity are the key ingredients for ferroelectric nanoscale topology.[22,23] Such strain effects can also significantly influence other ferroic orders, such as (anti)ferromagnetism. For instance, in antiferromagnets strain effects give rise to rich phase diagrams.[25,26]

Since strain and interfacial effects tune both ferroelectricity and magnetism, one may envisage that these strain and interface effects in *multiferroics* – materials with coexisting ferroic and magnetic orders – can affect both ferroic orders, and even the magnetoelectric coupling. Some imminent examples of this include electric control of the (anti-) ferromagnetic order driven by the interface coupling of both order parameters,[27] interface strain enhanced multiferroism,[28] ferroelastic switching of magnetoelectric order,[29] electrostatic modulation of the magnetic order parameter,[30,31] finite size effects on the magnetic long range order,[32] *etc*.

Here, we explore this concept further using $BiFeO_3$ (BFO) thin films.[33] BFO is a popular multiferroic and has been widely studied as it is one of the rare examples that retains it multiferroism at room temperature.[34] BFO thin films and nanostructures have shown many other attractive properties such as

optical functionality,[4] strain-dependent ferroelectric,[35] photoelectrochemical,[36] and magnetic response.[25] These functionalities are heavily underpinned by the domain morphology, and hence studies on the nanoscale control of the domain structure have attracted attention.[19,37–40]

While the domain arrangement for BFO films grown by excimer pulsed laser deposition (PLD) is typically stripe-like, it has been found that BFO films fabricated by frequency-tripled Nd:YAG laser (wavelength λ = 355 nm) consistently exhibit mosaic domains.[41–43] Here, we investigate the origins of such observations, *i.e.* despite identical mechanical and electrical boundary conditions, why such drastically different nanoscale domain topologies form. We show that the growth subtleties (likely related to the rapid growth rate[42]) of the Nd:YAG laser PLD system induces an out-of-plane strain gradient over a 5 nm length scale directly above the substrate. This gradient of $\sim 10^7$ m^{-1} effectively decouples the film from the substrate, and, despite the film's average strain being consistent, the film quality is reduced (with increased mosaicity), and mosaic domains are formed. For films grown by excimer laser, the strain is preserved coherently across the interface and the crystalline quality of the film can thus approach that of the substrate. Remarkably, we find that a careful annealing step can rearrange the strain state at the interface, converting the as-grown mosaic domains to stripe-like domains. The domain structure also affects the magnetic order in the BFO: we find that the smaller length scale of the domains in the mosaic domain samples induces a strong anharmonicity in the long-range spin cycloid.

Results and Discussion

Film Structural Properties

BFO is rhombohedral in the bulk, therefore when grown on (001)$_{pc}$ (pc = pseudocubic) oriented substrates the symmetry is typically reduced to monoclinic, and eight possible polarization variants (pointing along the body diagonals of the pseudocubic unit cell) exist. The specific domain structure can be controlled using vicinal miscut substrates, by using the substrate symmetry, and/or the properties of the lower electrode, allowing well-ordered stripes of 71˚ to 109˚ walls to be stabilized.[19,44,45] This has been achieved using, for instance, an excimer laser for ablation and DyScO$_3$ (DSO) (110)$_o$ (o = orthorhombic) substrates.

Here, we use BFO films grown using two different pulsed laser deposition chambers to explore (notably) the influence of incident flux on the interfacial, structural, and functional properties of the resulting films (see **Experimental Section**). In the following, we focus on a representative sample from each chamber type. We denote the BFO//DSO film grown by *excimer* laser Sample A, while the BFO//DSO film grown by *Nd:YAG* laser is denoted Sample B. A further sample grown by *Nd:YAG* laser and then subject to an *ex-situ*

annealing step is denoted Sample C and is discussed later. To eliminate any possible thickness-dependent structural response, for Samples A-C the BFO thickness was fixed at ~40 nm.

We first inspect the crystallographic structure of the films [**Figure 1**]. For Sample A, the high-angle x-ray diffraction (XRD) θ-2θ scan [**Figure 1(a)**; red] demonstrates single-phase growth. Note also that the BFO film peaks remain narrow and maintain their intensity even at higher orders. The XRD rocking curve (RC) around the (002) reflection of BFO [**Figure 1(b)**; red], with full width at half maximum (FWHM) of 0.03° shows a level of crystalline perfection approaching that of the substrate, while the Williamson-Hall (W-H) plot[46] [**Figure 1(c)**; red], which gives an estimate of the average strain *gradient* in the out-of-plane direction, demonstrates an almost zero inhomogeneous strain. Finally, reciprocal space mapping (RSM) near the $(013)_{pc}$ and $(003)_{pc}$ reflections [**Figure 1(d)**; red] establish that the film is coherently strained to the substrate, and reveals the presence of two monoclinic domains (with identical in-plane lattice parameter), typical for BFO films grown on DSO by excimer laser.[33,47]

The XRD data for Sample B reveal a film of differing crystalline quality from Sample A. The θ-2θ pattern [**Figure 1(b)**; blue] shows single-phase growth; however, the BFO film peaks become progressively broader upon increasing order. The RC measurement around (002) [**Figure 1(b)**; blue], with FWHM an order of magnitude larger than that of Sample A, reveals that the film has a stronger mosaicity. The W-H plot [**Figure 1(c)**; blue] yields a value of inhomogeneous strain of 0.2 %, once again an order of magnitude larger than the corresponding value for Sample A. Finally, the XRD RSMs around the $(013)_{pc}$ and $(003)_{pc}$ reflections [**Figure 1(d)**; blue] reveal two peaks, which correspond to two monoclinic domains; however, in a different arrangement from that observed in Sample A. The domains are separated *horizontally* (in Q_y), rather than *vertically* (in Q_z) as seen in Sample A, implying that the film has formed 'tilting' domains[48,49] through the strain accommodation process. Evidence for this is given by the fact that the $(003)_{pc}$ BFO peak splits horizontally along Q_y which is the result of a tilting of the (00*l*) lattice planes and does *not* reflect strain relaxation. In other words, the film *is* coherently strained to the substrate. Briefly here, we mention that an *ex-situ* annealing step allows us to take Sample C (grown by Nd:YAG laser) and modify the structural properties almost completely back to that observed for films grown by excimer laser. More details are discussed later. For Samples A and B, the XRD data show that they are nominally 'strained', but the level of crystalline perfection and magnitude of strain gradient differ markedly, with Sample A being 'superior' to Sample B on both counts.
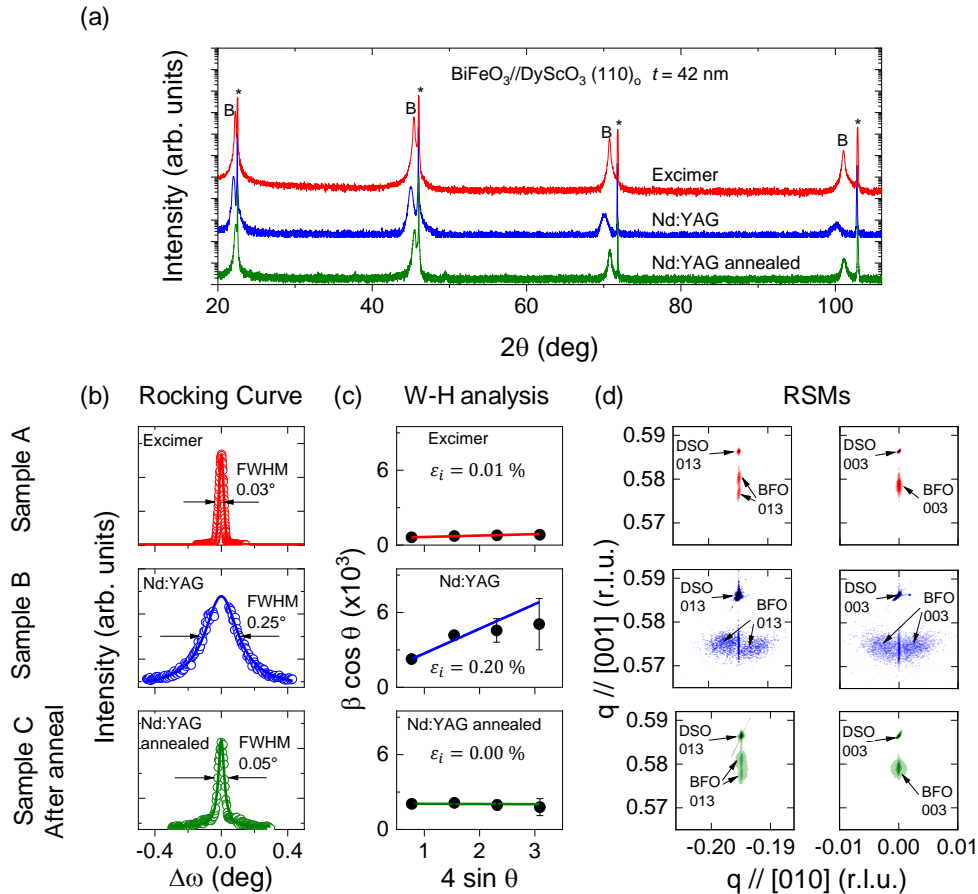
(a)

BiFeO$_3$//DyScO$_3$ (110)$_o$ t = 42 nm

Excimer

Nd:YAG

Nd:YAG annealed

2θ (deg)

Intensity (arb. units)

(b) Rocking Curve

(c) W-H analysis

(d) RSMs

Sample A

Sample B

Sample C After anneal

Excimer
FWHM 0.03°

Nd:YAG
FWHM 0.25°

Nd:YAG annealed
FWHM 0.05°

Intensity (arb. units)

Δω (deg)

Excimer
ε_i = 0.01 %

Nd:YAG
ε_i = 0.20 %

Nd:YAG annealed
ε_i = 0.00 %

β cos θ (x10^3)

4 sin θ

DSO 013 BFO 013

DSO 003 BFO 003

DSO 013 BFO 013

DSO 003 BFO 003

DSO 013 BFO 013

DSO 003 BFO 003

q // [001] (r.l.u.)

q // [010] (r.l.u.)

Figure 1. Structural characterization by x-ray diffraction (XRD). (a) High angle XRD θ-2θ scans of representative samples grown by excimer (red) and Nd:YAG laser (blue) and Nd:YAG laser with *ex-situ* annealing (green) (* = substrate; B = BFO). Film peak broadening at higher orders is much more pronounced for the Nd:YAG sample, but the peak intensity and width somewhat recovers after the annealing process. (b) Rocking curves (RC) around the (002)$_{pc}$ BFO reflection show a significant difference between the excimer (red) and Nd:YAG (blue) samples, while the Nd:YAG sample after annealing process (green) has a RC FWHM almost comparable to the excimer sample. (c) Out-of-plane Williamson-Hall (W-H) plots for the three sample types; showing that the as-grown state for Nd:YAG sample (blue) is a strong strain gradient, while the annealing step (green) can remove the strain gradient. (d) Asymmetric (013)$_{pc}$ (left) and symmetric (003)$_{pc}$ (right) XRD reciprocal space maps. For the excimer sample (red) the domain structure is precisely as commonly observed for BFO//DSO; while for the Nd:YAG sample (blue) the domain structure is slightly more complicated (see text). The annealing process on the Nd:YAG sample can recover the domain structure to a more ordered state (green), similar to the excimer case.

To probe the ferroelectric domain structure, we used piezoresponse force microscopy (PFM). The out-of-plane PFM phase (OPP) for Sample A [**Figure 2(a)**] shows a single contrast, consistent with a single out-of-plane ferroelectric variant. On the other hand, the OPP for Sample B [**Figure 2(b)**] shows both bright and dark contrast, implying the existence of two out-of-plane domain variants. The in-plane phase (IPP) image for

Sample A [**Figure 2(c)**] reveals well-ordered stripe-like domains,[45] while for Sample B, the mosaic domains observed in the OPP are also reflected in the IPP image [**Figure 2(d)**]. Critically, the characteristic domain sizes are very different for Samples A (stripe) and B (mosaic) – with the domains being at least 2-3 times smaller in the mosaic domain sample. It is suggested that the higher growth rate for Sample B is the reason for such disordered domains.[4,41,42,50–53] Note that Sample C, grown by Nd:YAG laser with as-grown mosaic domains [**Figure 2e-h)**], can be converted by annealing to show a striped domain arrangement (discussed later).

We point out that for samples A and B, the XRD data in **Figure 1** show that the out-of-plane lattice parameter are not identical. Therefore, to rule out the possibility that the *average* strain state in the films is responsible for the formation of stripe *vs*. mosaic domains, in **Figure S1** and **Figure S2** (Supporting Information) we show W-H analysis and PFM images for BFO samples grown on $SrTiO_3$ and $GdScO_3$ substrates, with larger compressive strain than DSO and virtually no strain, respectively. The general trend observed here is confirmed in these additional samples; that is, that PLD A films have almost zero strain gradient and stripe domains, while PLD B films are subject to a prominent strain gradient which induces mosaic domains.
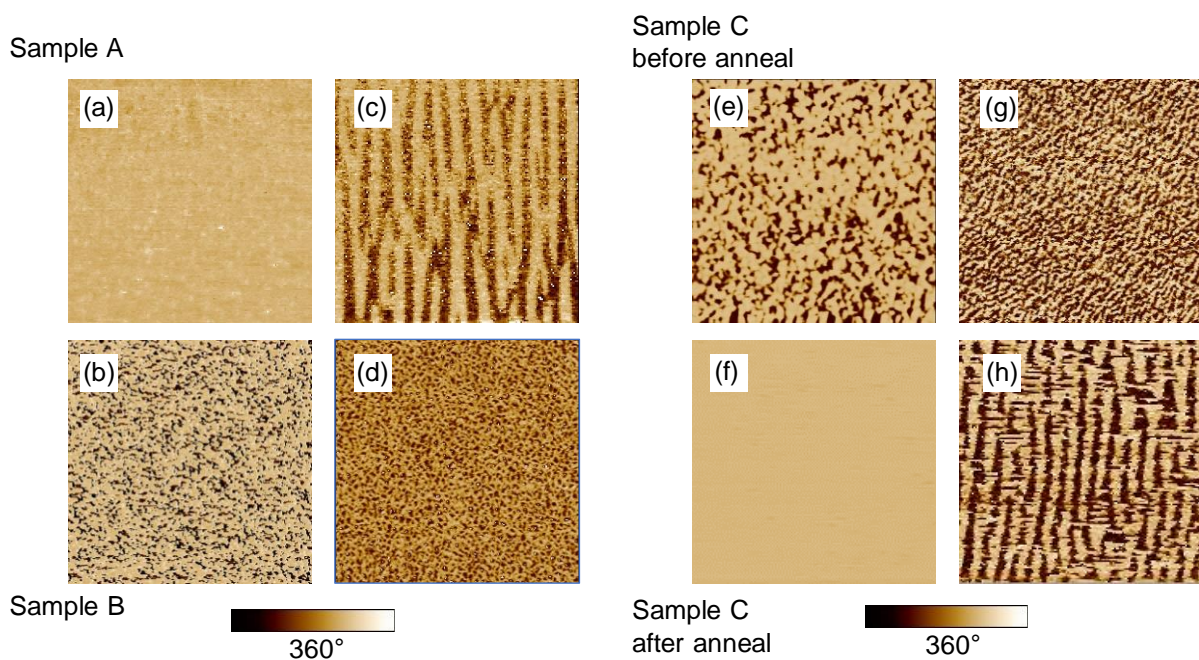

Figure 2. Piezoresponse force microscopy of various sample types. Out of plane PFM phase (OPP) images of (a) Sample A and (b) Sample B. In plane phase (IPP) images for (c) Sample A and (d) Sample B. Note that Sample A shows a clear well-ordered stripe domain structure, while Sample B shows more disordered mosaic domains. Converting from mosaic domains to stripe-like domains using *ex-situ* annealing. As-grown domain structure of Sample C: (e) OPP and (g) IPP. After the annealing, the OPP becomes uniform (f), and the in-plane domains form a much more ordered stripe-like structure (h), showing that Sample C after annealing becomes similar to Sample A. All micrographs are 3 µm by 3 µm.

Scanning Transmission Electron Microscopy

The preceding discussion showed that Samples A and B have significant differences in their crystallographic and ferroelectric domain structure. To understand exactly how and why mosaic domains are formed in Sample B, we used high-resolution scanning transmission electron microscopy (STEM). Data for Sample A are presented in **Figure 3(a-c)**. The high-angle annular dark field (HAADF) image [**Figure 3(a)**] demonstrates a highly coherent film on the substrate (images taken on the other zone axis give very similar results – data not shown). To understand these strain profiles at the nanoscale, geometric phase analysis (GPA) mapping was performed. The in-plane strain (reported here relative to the DSO substrate) ε_{xx} [**Figure 3(b)**] reveals a clear coherence between film and substrate with the value remaining zero in both the substrate and film regions. On the other hand, the out-of-plane strain ε_{yy}, [**Figure 3(c)**] shows a distinct jump from 0 % in the DSO substrate to +1.2 % in the BFO film. Such a level of tensile strain is expected for BFO//DSO since the in-plane biaxial misfit strain is of the order of -0.4 % (compressive). Therefore, Sample A is fully strained and coherent to the substrate, with almost no strain gradient in both the out-of-plane and in-plane directions.
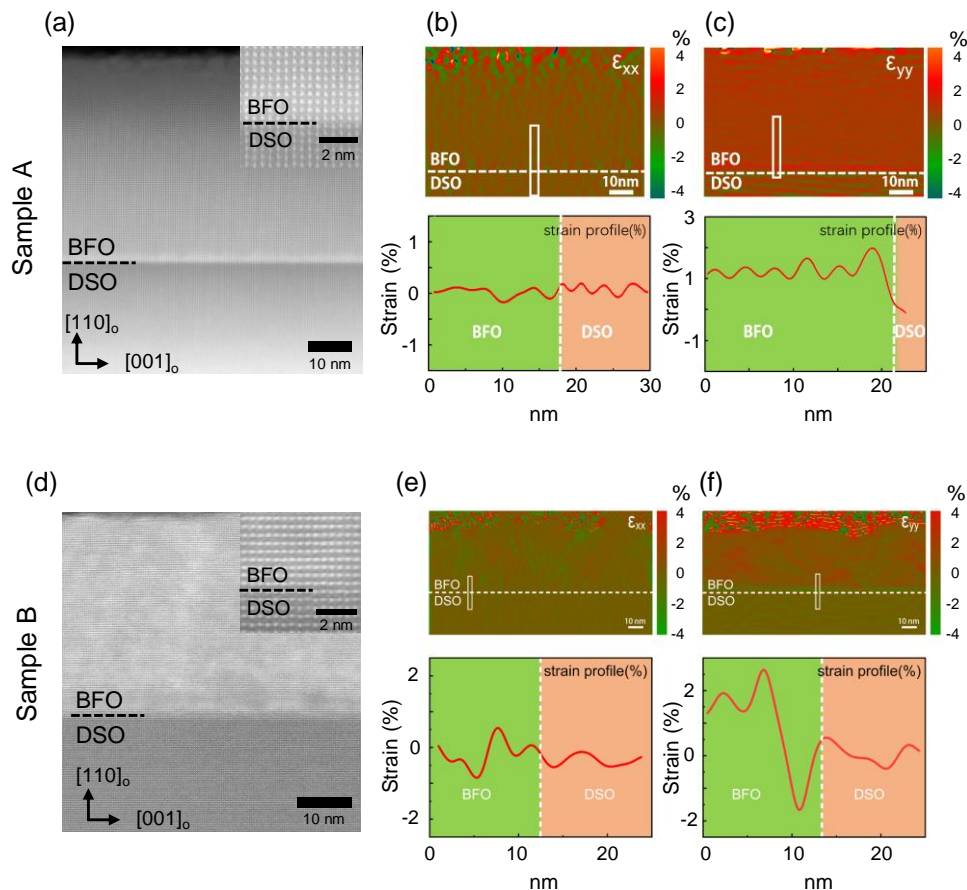

Figure 3. Determination of strain profiles by HAADF-STEM imaging. (a-c) HAADF image, in-plane strain (ε_{xx}), out-of-plane strain (ε_{yy}) and corresponding line profiles of marked areas for Sample A (excimer). (d-f) HAADF image, in-plane strain (ε_{xx}), out-of-plane strain (ε_{yy}) and corresponding line profiles of marked areas for Sample B (Nd:YAG).

On the other hand, the STEM results for Sample B shed some important light on its structural characteristics. Like Sample A, the STEM image [**Figure 3(d)**] demonstrates a film that is coherently grown on the substrate, and the in-plane strain profile [**Figure 3(e)**] is centered around zero. The out-of-plane strain profile [**Figure 3(f)**], however, shows an important difference. Remarkably, in the first few nanometers of the film (just above the substrate), the out-of-plane strain decrease abruptly to -1.5 % for about 2-3 nm, before it increases to ~1.5 % at about 6 nm from the interface. Such an observation is particularly striking, since in the same region there is no appreciable change in the in-plane strain. This kind of interfacial, local *uniaxial* distortion of the BFO unit cell suggests either a chemical interdiffusion effect, stoichiometry change, or some other oxygen octahedra distortion-related effects such as screening of the polarization.
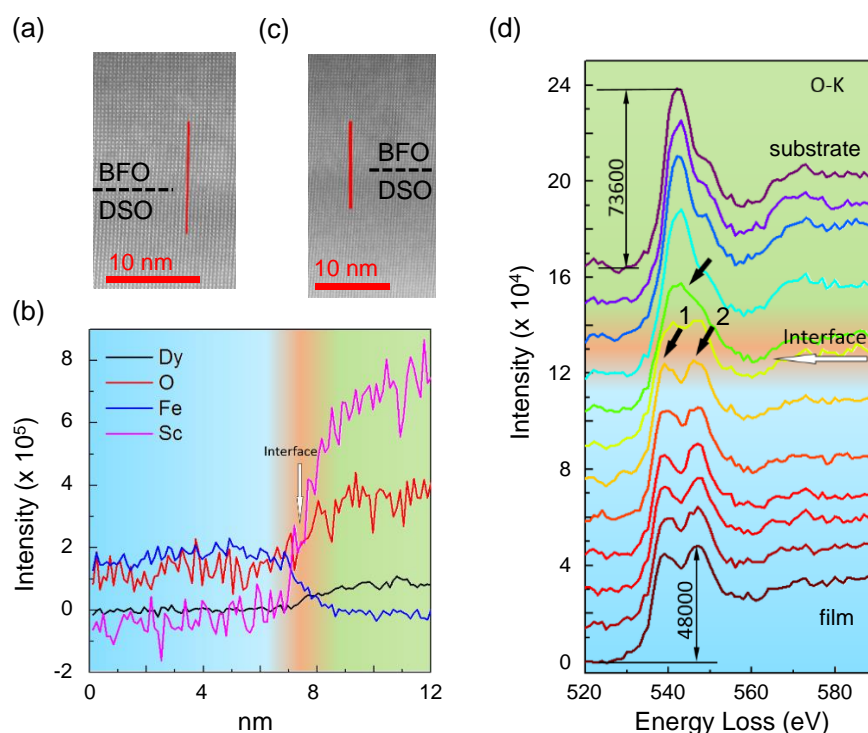

Figure 4. Electron energy loss spectroscopy (EELS) results on the BFO//DSO film grown by Nd:YAG laser (Sample B). HAADF image (a) and corresponding element distribution (b) along the red line in (a), showing a clear interface within 2 nm along the heterostructure. HAADF image (c) and corresponding oxygen K-edge evolution (d) along the red line in (c) shows that at the interface a change in peak structure occurs, possibly related to a coordination / stoichiometry change at the interface.

To probe this further, we acquired electron energy loss spectroscopy (EELS) line scans of Sample B to search for possible stoichiometry and/or oxygen environment changes. The elemental distribution along the red line in **Figure 4(a)** shows a clear drop to zero within 1 nm for Dy and Sc when going from the substrate to film [**Figure 4(b)**]. Meanwhile, the intensities for Fe (and O) show a clear drop (increase) from film to substrate

within 1 nm [**Figure 4(b)**]. These results allow us to rule out the influence of stoichiometry as the origin of the strange strain profile. One could imagine that antisites could be responsible for the interfacial gradient; however, given the uniform strain profile over the entire interface (we checked the profile at various locations on the sample), and the fact that we do not observe strain fields in other parts of the film, allows us to suggest that antisites are not the dominant factor at play in our case. We cannot, however, rule out the possible segregation of antisites to the interfacial region which could potentially result in such a gradient. On the other hand, the oxygen coordination shows some dependence on the position relative to substrate/film interface. The electron energy-loss near edge structures (ELNES) of the oxygen K-edge are sensitive to chemical bonding and may give us a hint for electronic structure changes.[54,55] The oxygen K-edge evolution along the red line in **Figure 4(c)** shows that at the interface a change in peak structure occurs [**Figure 4(d)**]. Peaks 1 and 2 (at ~539 and ~547 eV respectively) in the BFO film have comparable intensity; however, in the DSO substrate, peak 1 is more intense than peak 2. At the interface, the oxygen K-edge gradually changes within 2-3 nm, consistent with the strong decrease of strain observed in **Figure 3(f)**. The ELNES of the oxygen K edge is reported to relate to structural distortions of oxygen octahedra in perovskites.[56] According to this, the strong modification of the O-K peak structure at the interface may also correspond to a change in the oxygen coordination across the interface. Since the crystal field splitting and hybridization is dependent on the distortion of the oxygen octahedra,[57] a change in the oxygen coordination would affect the polarization displacement and hence the axial ratio.[58] This is consistent with the strain profile behavior as described above.

Controlled Annealing to Convert Mosaic Domains to Stripe Domains

Now that we have shown that the differences in the growth parameters between the excimer and Nd:YAG grown samples induce dramatic changes in the strain profile and thus the domain structure, the next question was to determine if indeed the mosaic domain structure was 'locked in', *i.e.* could some treatment process recover the sample so that the film showed stripe like domains? We were motivated to explore this by a recent work from Nahas *et al.* in which a labyrinthine domain pattern (disordered stripe domains with topological defects) of ferroelectric domains in BFO films could be converted to a perfectly ordered stripe domain pattern with lengths of over several tens of microns.[59] Such changes were experimentally obtained by an *ex situ* annealing process whereby the sample was held at 1073 K for 1 hour under oxygen flow and cooled down slowly to room temperature (2 K min^{-1}).

We applied this same annealing procedure to Sample C, a 42 nm Nd:YAG -fabricated BFO film with as-grown mosaic domains. We then measured its structural properties with XRD and the domain arrangement with PFM. First, the crystallinity of the film is improved, as evidenced by the XRD data: the θ-2θ pattern shows rather sharp peaks even up to higher orders [**Figure 1(a)**; green]; the rocking curve around the $(002)_{pc}$

reflection [**Figure 1(b)**; green] is closer in FWHM to the curves shown for the excimer sample, the W-H analysis shows a negligible strain gradient [**Figure 1(c)**; green], and finally the domain structure is completely rearranged, with the tilting domains completely removed [**Figure 1(d)**; green]. These observations would strongly suggest that the annealing step has caused a complete rearrangement of the strain profile at the interface. Indeed, the annealing process has converted the mosaic domains to well-ordered stripe domains [**Figure 2(e-f)** OPP, and **2(g-h)** for IPP]. Interestingly, whereas the surface before annealing had a rough topography, the sample surface becomes a clear stepped structure after annealing [**Figure S1, Supporting Information**]. These results unambiguously demonstrate that the annealing step reduces structural disorder of the film and therefore allows the substrate strain to be coherently imposed, just as is the case for excimer-grown samples, thus inducing stripe-like domain structures.

Influence of Domain Structure on Magnetic Order

Next, we consider the influence of a mosaic domain structure on the magnetic order in BFO films. Since, as mentioned above, BFO is multiferroic, one may consider the possibility that such a large interfacial strain gradient and the related mosaic domain structure can influence the magnetic order. A unique feature of BFO in the bulk (and in weakly-strained films) is the presence of a long-period spin cycloid.[60] The length of this cycloid in films is typically $\lambda \approx 70\text{-}80$ nm (Refs. [32,47,61]), and various works have considered the so-called 'anharmonicity' of the cycloid.[62] Anharmonicity refers to a 'bunching' of the spins towards a preferred direction, usually induced by an external magnetic field or by a strain induced anisotropy. Since the characteristic length of the cycloid is of the order of domain sizes in thin films, one may expect that a less ordered domain structure could destabilize this long-range magnetic arrangement.

To explore such a possibility, we grew ^{57}Fe-enriched BFO films on DSO substrates using the same growth chambers as used for Samples A and B. Samples D and E were grown using excimer and Nd:YAG laser, respectively, to a thickness of 25 nm. Characterization by x-ray diffraction (not shown) evidences similar crystallinity differences between the samples as was observed for Samples A and B.

^{57}Fe conversion electron Mössbauer spectroscopy (CEMS) is a powerful technique to probe the magnetic structure of iron-containing thin films. It probes the magnetic environment of the Fe^{3+} ions, and allows to distinguish between various types of magnetic arrangements such as cycloidal and/or collinear antiferromagnetic, based on analysis of the shape and line intensities of the Mössbauer spectrum.[26,53,63,64] In this work, we performed CEMS measurements at room temperature with the γ-ray incident normally to the sample. The collected spectra exhibit magnetic Zeeman-split sextets with isomer shift ($\delta \sim 0.38$ mm.s^{-1}) and hyperfine field values ($B_{hf} \sim 48.8$ T) typical of Fe^{3+} ions in octahedral coordination.

The CEMS spectrum collected for Sample D (with striped domains) [**Figure 5(a)**] exhibits a clear asymmetry: note that the intensity of the 1st and 6th peaks (when counted from the left) are rather different, as are the 2nd and 5th peaks. As discussed in detail in Refs. [53,65], such an asymmetry in the spectrum suggests that the magnetic arrangement is more complex than simple collinear antiferromagnetism. Guided by previous observations for films under similar levels of strain,[47,66] we have successfully fit the spectrum with a model corresponding to a (slightly) anharmonic cycloid (with anharmonicity along the propagation direction, and parameter of $m = 0.5$) with a tilting of the cycloid plane (of about 5 degrees) toward in the in-plane direction (full details given in the **Supporting Information**).
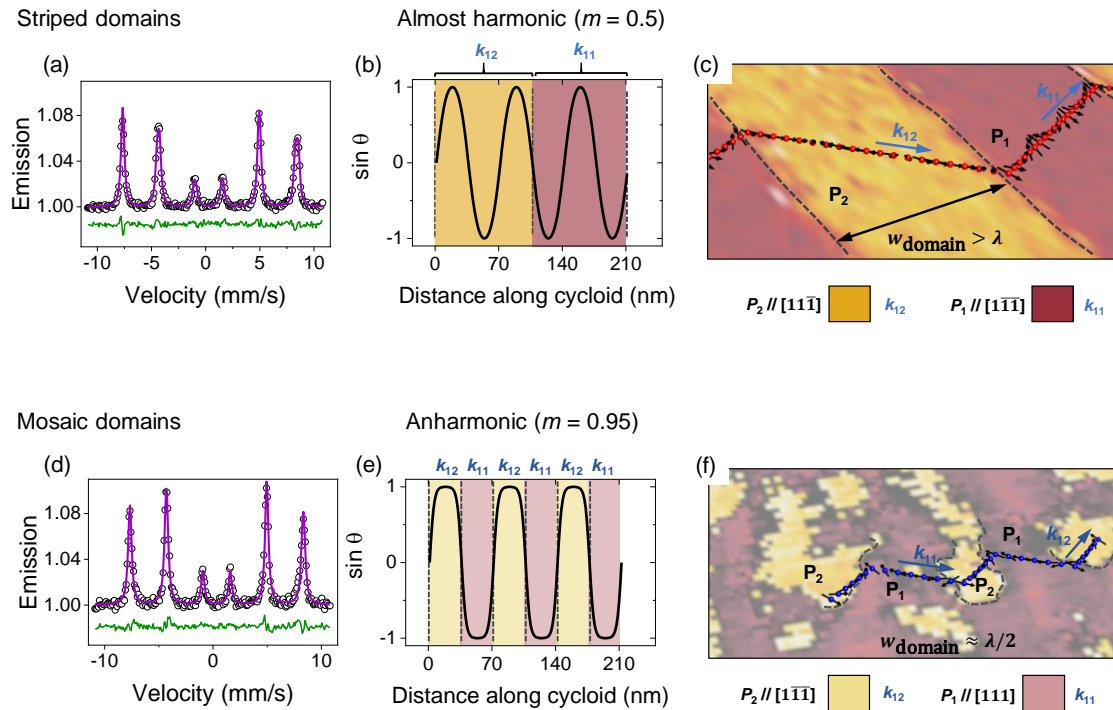

Figure 5. Influence of domain structure on the magnetic cycloid in BFO films. CEMS spectrum collected at 295 K for Sample D (striped domains) (a) and Sample E (mosaic domains) (d). The spectra are fit with models based on cycloidal spin orders with various anharmonicity parameters (as described in **Supporting Information**). For the striped domain arrangement, the best fit is found for an almost harmonic cycloid, for which $\sin \theta$ is plotted (where θ is angle between the spin direction and **P**) in (b). The low value of the anharmonicity parameter m implies a smooth rotation of the spins throughout the cycloid period. (c) Schematic of possible cycloidal arrangement for striped domain samples with PFM image underneath. In each domain, the cycloid has about 1.5 periods to propagate unperturbed before having to change propagation direction (i.e. from k_{12} to k_{11}). On the other hand, the mosaic domain arrangement with smaller domain sizes of about 30-40 nm give rise to a more anharmonic cycloid ($m = 0.95$) in which, within the domain the spins are predominantly in plane, and in the vicinity of the walls the spins undergo most of the cycloid rotation, as demonstrated by the behavior of $\sin \theta$ (e). (f) Schematic of possible spin arrangements for the strongly anharmonic cycloid in mosaic domain samples. Note here that a single cycloid period in fact straddles two FE domains, and that within the 'bulk' part of the domains the spins are almost completely 'flat' – *i.e.* in the film plane.

On the other hand, the spectrum for Sample E [**Figure 5(d)**] is almost symmetric, with the relative intensities (normalized to the central lines) of the 1st, 2nd, and 3rd peaks close to 3, 4, and 1, respectively. Such an observation is consistent with a spin arrangement in which the direction of hyperfine field B_{hf} for each spin site makes an angle of ~90 degrees to the incident γ-ray direction, in other words, the spins are predominantly confined to the film plane. To fit the data, we have considered separately various spin arrangements: collinear antiferromagnetic with the spins in the plane, as well as various types of cycloids with different tilting patterns, and combinations thereof (details are given in **Supporting Information**). The integrated error for the various fit types suggests that Sample E is best described as having an anharmonic cycloid ($m = 0.95$) with the cycloid plane tilted about 20 degrees from the film plane.

Therefore, Samples D and E have magnetic order that depends on the ferroelectric domain arrangement. Since the propagation vector of the spin cycloid is 'locked' to a specific polarization direction [shown in **Figure 5(c)**], the propagation direction changes when one passes from one domain to the next. As first shown using real space magnetometry techniques for BFO//DSO (Ref. [47]), for the well-ordered stripe-like domains the cycloid has the possibility to propagate relatively uninhibited within the ferroelectric stripes [**Figure 5(c)**]. The stripe periodicity for our 25 nm thick film is estimated to be 81 nm, and since the cycloid propagates at 45 degrees to the domain walls, this implies that in each domain, the cycloid has ~114 nm (or ~1.5 periods) to propagate before changing direction [**Figure 5(c)**]. The influence of the weak anharmonicity is shown in **Figure 5(b)**, where the value of sin θ is plotted as a function of distance. θ is the angle that the spin subtends with the direction of the FE polarization: if sin θ = 0 the spin is close to aligned along the **P** direction; while if sin θ = ±1 then the spin is oriented orthogonal to **P**; in this case, in the film plane. Note that in **Figure 5(b)** the value of sin θ appears to oscillate in a similar fashion to a sine function. This is because the anharmonicity ($m = 0.5$) is not enough to show a noticeable difference from a normal sine function (see full details in **Supporting Information**). The schematic in **Figure 5(c)** shows that the Fe spins can rotate relatively unperturbed for more than a whole cycloid period within the domains before hitting a domain wall and changing propagation direction.

For the mosaic domain structure, the higher level of disorder makes it more difficult to determine a solid characteristic domain size; however, FFT analyses of PFM images allow us to estimate the domains to be ~40 nm. Now, a prominent anharmonicity in the cycloid, particularly when the parameter m → 1, causes the cycloid to become 'domain-like' which implies that for the most part of the cycloid propagation, the spins are confined approximately to a particular direction (that is, sin θ = ± 1, implying that the spins are almost confined to the film plane), while in the vicinity of domain walls the spins rapidly rotate to complete the cycloid.[67] In this case, the magnetic domain size is approximately twice the ferroelectric domain size, as schematically illustrated in **Figure 5(e,f)**. Note that the FE domain sizes in Sample E are about 40 nm, while the cycloid period

is expected to remain (based on the average strain level) approximately 70-80 nm.[47,61] Therefore, in Sample E, the cycloid is perturbed by the presence of the disordered domain walls and becomes strongly anharmonic.

These results thus demonstrate that interfacial strain gradients, through their effect on the domain structure, directly influence the magnetic ordering in BFO films. Since typically strain and magnetic fields are used to tailor the anharmonicity of this spin arrangement, here we have shown that the significant increase in anharmonicity from striped domains to mosaic domains gives another handle to tweak the spin cycloid in BFO.

Conclusions

In summary, we have shown that interfacial strain gradients can influence the nanoscale domain morphology in epitaxial BFO films. The key findings of this study are the following:

i. By taking advantage of differences in growth kinetics for two different PLD chambers, we showed that high flux growth can be exploited to induce large strain gradients at the film-substrate interface.

ii. An extremely localized strain gradient can decouple the film from the substrate and thus disrupt long-range order, inducing mosaic domains. On the other hand, films grown coherently with no interfacial strain gradient exhibit typical stripe-like domains. Controlled annealing of a BFO film with as-grown mosaic domains removes the strain gradient and converts the domains from mosaic to striped.

iii. Concomitant changes in the magnetic structure of the films are revealed, with the striped domain structure giving rise to a cycloidal order with low anharmonicity parameter; while the mosaic domain arrangement induces significant anharmonicity in the cycloid due to the disorder of the higher density of domain walls.

These results demonstrate that atomic scale tuning of interfacial strain gradients can be a powerful route to manipulate the global ferroelectric and magnetic order in multiferroic thin films.

Experimental Section

Fabrication of BiFeO₃ heterostructures: Epitaxial $BiFeO_3$ thin films were grown by pulsed laser deposition. Three growth chambers were used, the respective growth conditions of which can be found in Refs. [47,68,69].

X-ray Diffraction and Williamson-Hall Plot Analysis: Structural characterization was performed by x-ray diffraction using an MRD 'Xpert Pro diffractometer using Cu $K_{\alpha-1}$ radiation. To estimate the average strain gradient across the entire BFO film thickness, we used the θ-2θ scans of 001, 002, 003, and 004 reflections and followed the procedure outlined in Refs. [5,46]. For Sample B, the value of inhomogeneous strain ε_i = 0.2 % allows us to estimate a strain gradient of 1.7×10^5 m⁻¹ across the whole film thickness (assuming an exponential strain profile). Note that the *interfacial* strain gradient is much larger when computed using the TEM data of **Figure 3**. Namely, a strain change of ~4 % over a distance of ~5 nm is found, yielding a gradient of ~10^7 m⁻¹. Although these values vary by some orders of magnitude, this is unsurprising as the TEM method uses only the interfacial region while the XRD method considers the entire film thickness.

Piezoresponse Force Microscopy: The ferroelectric domain structure was probed by PFM using a commercial Asylum Cypher atomic force microscope. The in-plane and out-of-plane domain images were captured using Pt/Cr coated tips (Budget sensors), 75 kHz, ~3N m⁻¹ with an AC excitation voltage at 75 kHz of ~500 mV. Further experiments used an atomic force microscope (Nanoscope V multimode, Bruker) and two external lock-in detectors (SR830, Stanford Research) for the simultaneous acquisition of in-plane and out-of-plane responses. An external ac source (DS360, 379 Stanford Research) was used to excite the PFM tip at 35 kHz. Stiff cantilevers (40 N.m⁻¹) were used for accurate out-of-plane detection and softer tips (3-7 N m⁻¹) for in-plane detection.

Scanning Transmission Electron Microscopy: HAADF-STEM and EELS data were acquired using a Titan Cubed 60-300kV aberration-corrected scanning transmission electron microscope. The microscope is equipped with double aberration correctors from CEOS, a high-brightness field-emission gun, a monochromator and a GIF Quantum ER system (the energy resolution can reach 0.2 eV) operating at 300 kV. HAADF-STEM images were recorded at a convergence semi-angle of 21.4 mrad and a collection angle of 50-250 mrad. Strain analyses were carried out using GPA plugins based on the Gatan Digital Micrograph platform. EELS data were acquired with a dispersion of 1.0 eV ch⁻¹ and an entrance aperture of 5 mm.

Conversion Electron Mössbauer Spectroscopy (CEMS): CEMS spectra were recorded in normal incidence using a home-made He-5% CH_4 gas flow proportional counter[70] and a 1.5 GBq ^{57}Co source in a Rh matrix in constant acceleration mode. The spectra were fitted with the MOSFIT code using the histogram method (full details are given in the **Supporting Information**). Isomer shifts are given with respect to α-Fe at 300 K.

Acknowledgements

Conflict of Interest: The authors declare no conflict of interest.

References

[1]   A. von Hippel, *Rev. Mod. Phys.* **1950**, *22*, 221.

[2]   J. G. Bednorz, K. A. Müller, *Rev. Mod. Phys.* **1988**, *60*, 585.

[3]   B. W. Wessels, *Annu. Rev. Mater. Res.* **2007**, *37*, 659.

[4]   D. Sando, P. Hermet, J. Allibe, J. Bourderionnet, S. Fusil, C. Carrétéro, E. Jacquet, J.-C. Mage, D. Dolfi, A. Barthélémy, P. Ghosez, M. Bibes, *Phys. Rev. B* **2014**, *89*, 195106.

[5]   D. Sando, Y. Yang, C. Paillard, B. Dkhil, L. Bellaiche, V. Nagarajan, *Appl. Phys. Rev.* **2018**, *5*, 041108.

[6]   D. Sando, Y. Yang, E. Bousquet, C. Carrétéro, V. Garcia, S. Fusil, D. Dolfi, A. Barthélémy, P. Ghosez, L. Bellaiche, M. Bibes, *Nat. Commun.* **2016**, *7*, 10718.

[7]   A.-M. H. Gosnet, J.-P. Renard, *J. Phys. D. Appl. Phys.* **2003**, *36*, R127.

[8]   F. Y. Bruno, K. Z. Rushchanskii, S. Valencia, Y. Dumont, C. Carrétéro, E. Jacquet, R. Abrudan, S. Blügel, M. Ležaić, M. Bibes, A. Barthélémy, *Phys. Rev. B* **2013**, *88*, 195108.

[9]   K. J. Choi, M. Biegalski, Y. Li, A. Sharan, J. Schubert, R. Uecker, P. Reiche, Y. Chen, X. Pan, V. Gopalan, L.-Q. Chen, D. G. Schlom, C.-B. Eom, *Science* **2004**, *306*, 1005.

[10]   L. Chen, Y. Yang, Z. Gui, D. Sando, M. Bibes, X. K. Meng, L. Bellaiche, *Phys. Rev. Lett.* **2015**, *115*, 267602.

[11]   M. N. Grisolia, F. Y. Bruno, D. Sando, H. J. Zhao, E. Jacquet, X. M. Chen, L. Bellaiche, A. Barthélémy, M. Bibes, *Appl. Phys. Lett.* **2014**, *105*, 172402.

[12]   M. E. Lines, A. M. Glass, *Principles and Applications of Ferroelectrics and Related Materials*; 1977.

[13]   P. Lacorre, J. Pannetier, S. A. I. Nazzal, P. W. Wang, T. C. Huang, *J. Solid State Chem.* **1991**, *91*, 225.

[14]   O. V. M. Goldschmidt, *Naturwissenschaften* **1926**, *14*, 477.

[15]   M. Ahart, M. Somayazulu, R. E. Cohen, P. Ganesh, P. Dera, H. Mao, R. J. Hemley, Y. Ren, P. Liermann, Z. Wu, *Nature* **2008**, *451*, 1.

[16]   D. G. Schlom, L.-Q. Chen, C. J. Fennie, V. Gopalan, D. A. Muller, X. Pan, R. Ramesh, R. Uecker, *MRS Bull.* **2014**, *39*, 118.

[17]   A. Ohtomo, H. Y. Hwang, *Nature* **2004**, *427*, 423.

[18]   M. N. Grisolia, J. Varignon, G. Sanchez-Santolino, A. Arora, S. Valencia, M. Varela, R. Abrudan, E.

Weschke, E. Schierle, J. E. Rault, J. P. Rueff, A. Barthélémy, J. Santamaria, M. Bibes, *Nat. Phys.* **2016**, *12*, 2.

[19] Y. H. Chu, Q. He, C. H. Yang, P. Yu, L. W. Martin, P. Shafer, R. Ramesh, *Nano Lett.* **2009**, *9*, 1726.

[20] Y. J. Shin, B. C. Jeon, S. M. Yang, I. Hwang, M. R. Cho, D. Sando, S. R. Lee, J. G. Yoon, T. W. Noh, *Sci. Rep.* **2015**, *5*.

[21] Q. Zhang, L. Xie, G. Liu, S. Prokhorenko, Y. Nahas, X. Pan, L. Bellaiche, A. Gruverman, N. Valanoor, *Adv. Mater.* **2017**, *29*, 1702375.

[22] Y. L. Tang, Y. L. Zhu, X. L. Ma, A. Y. Borisevich, A. N. Morozovska, E. A. Eliseev, W. Y. Wang, Y. J. Wang, Y. B. Xu, Z. D. Zhang, S. J. Pennycook, *Science* **2015**, *348*, 547.

[23] A. K. Yadav, C. T. Nelson, S. L. Hsu, Z. Hong, J. D. Clarkson, C. M. Schlepuëtz, A. R. Damodaran, P. Shafer, E. Arenholz, L. R. Dedon, D. Chen, A. Vishwanath, A. M. Minor, L. Q. Chen, J. F. Scott, L. W. Martin, R. Ramesh, *Nature* **2016**, *530*, 198.

[24] A. M. George, J. Íñiguez, L. Bellaiche, *Nature* **2001**, *413*, 54.

[25] D. Sando, A. Agbelele, C. Daumont, D. Rahmedov, W. Ren, I. C. Infante, S. Lisenkov, S. Prosandeev, S. Fusil, E. Jacquet, C. Carretero, S. Petit, M. Cazayous, J. Juraszek, J.-M. Le Breton, L. Bellaiche, B. Dkhil, A. Barthelemy, M. Bibes, *Philos. Trans. R. Soc. A* **2014**, *372*, 20120438.

[26] D. Sando, F. Appert, B. Xu, O. H. C. Paull, S. R. Burns, C. Carrétéro, B. Dupé, V. Garcia, Y. Gallais, A. Sacuto, M. Cazayous, B. Dkhil, J.-M. Le Breton, A. Barthélémy, M. Bibes, L. Bellaiche, V. Nagarajan, J. Juraszek, *Appl. Phys. Rev.* **2019**, *041404*.

[27] T. Zhao, A. Scholl, F. Zavaliche, K. Lee, M. Barry, A. Doran, M. P. Cruz, Y. H. Chu, C. Ederer, N. A. Spaldin, R. R. Das, D. M. Kim, S. H. Baek, C. B. Eom, R. Ramesh, *Nat. Mater.* **2006**, *5*, 823.

[28] J. A. Mundy, C. M. Brooks, M. E. Holtz, J. A. Moyer, H. Das, A. F. Rébola, J. T. Heron, J. D. Clarkson, S. M. Disseler, Z. Liu, A. Farhan, R. Held, R. Hovden, E. Padgett, Q. Mao, H. Paik, R. Misra, L. F. Kourkoutis, E. Arenholz, A. Scholl, J. A. Borchers, W. D. Ratcliff, R. Ramesh, C. J. Fennie, P. Schiffer, D. A. Muller, D. G. Schlom, *Nature* **2016**, *537*, 523.

[29] S. H. Baek, H. W. Jang, C. M. Folkman, Y. L. Li, B. Winchester, J. X. Zhang, Q. He, Y. H. Chu, C. T. Nelson, M. S. Rzchowski, X. Q. Pan, R. Ramesh, L. Q. Chen, C. B. Eom, *Nat. Mater.* **2010**, *9*, 309.

[30] C. A. F. Vaz, J. Hoffman, C. H. Ahn, R. Ramesh, *Adv. Mater.* **2010**, *22*, 2900.

[31] C. A. F. Vaz, J. Hoffman, Y. Segal, J. W. Reiner, R. D. Grober, Z. Zhang, C. H. Ahn, F. J. Walker, *Phys. Rev.*

Lett. **2010**, *104*, 127202.

[32]   S. R. Burns, D. Sando, B. Xu, B. Dupé, L. Russell, G. Deng, R. Clements, O. H. C. Paull, J. Seidel, L. Bellaiche, N. Valanoor, C. Ulrich, *NPJ Quantum Mater.* **2019**, *4*, 18.

[33]   D. Sando, A. Barthélémy, M. Bibes, *J. Phys. Condens. Matter* **2014**, *26*, 473201.

[34]   G. Catalan, J. F. Scott, *Adv. Mater.* **2009**, *21*, 2463.

[35]   I. C. Infante, S. Lisenkov, B. Dupé, M. Bibes, S. Fusil, E. Jacquet, G. Geneste, S. Petit, A. Courtial, J. Juraszek, L. Bellaiche, A. Barthélémy, B. Dkhil, *Phys. Rev. Lett.* **2010**, *105*, 057601.

[36]   F. Gao, X. Chen, K. Yin, S. Dong, Z. Ren, F. Yuan, T. Yu, Z. Zou, J. M. Liu, *Adv. Mater.* **2007**, *19*, 2889.

[37]   N. Balke, S. Choudhury, S. Jesse, M. Huijben, Y. H. Chu, A. P. Baddorf, L. Q. Chen, R. Ramesh, S. V Kalinin, *Nat. Nanotechnol.* **2009**, *4*, 868.

[38]   L. W. Martin, Y.-H. Chu, M. B. Holcomb, M. Huijben, P. Yu, S. Han, D. Lee, S. X. Wang, R. Ramesh, *Nano Lett.* **2008**, *8*, 2050.

[39]   C. J. M. Daumont, S. Farokhipoor, A. Ferri, J. C. Wojdeł, J. Íñiguez, B. J. Kooi, B. Noheda, *Phys. Rev. B* **2010**, *81*, 144115.

[40]   D. Zhang, D. Sando, P. Sharma, X. Cheng, F. Ji, V. Govinden, M. Weyland, V. Nagarajan, J. Seidel, *Nat. Commun.* **2020**, *11*, 5.

[41]   G. Catalan, H. Béa, S. Fusil, M. Bibes, P. Paruch, A. Barthélémy, J. Scott, *Phys. Rev. Lett.* **2008**, *100*, 027602.

[42]   D. Sando, C. Carrétéro, M. N. Grisolia, A. Barthélémy, V. Nagarajan, M. Bibes, *Adv. Opt. Mater.* **2017**, *6*, 1700836.

[43]   Y. H. Jang, C. H. Kim, S. J. Seo, J. H. Cho, *Thin Solid Films* **2013**, *548*, 52.

[44]   H. W. Jang, D. Ortiz, S.-H. Baek, C. M. Folkman, R. R. Das, P. Shafer, Y. Chen, C. T. Nelson, X. Pan, R. Ramesh, C.-B. Eom, *Adv. Mater.* **2009**, *21*, 817.

[45]   Y.-H. Chu, Q. Zhan, L. W. Martin, M. P. Cruz, P.-L. Yang, G. W. Pabst, F. Zavaliche, S.-Y. Yang, J.-X. Zhang, L.-Q. Chen, D. G. Schlom, I.-N. Lin, T.-B. Wu, R. Ramesh, *Adv. Mater.* **2006**, *18*, 2307.

[46]   B. C. Jeon, D. Lee, M. H. Lee, S. M. Yang, S. C. Chae, T. K. Song, S. D. Bu, J.-S. Chung, J.-G. Yoon, T. W. Noh, *Adv. Mater.* **2013**, *25*, 5643.

[47]   I. Gross, W. Akhtar, V. Garcia, L. J. Martínez, S. Chouaieb, K. Garcia, C. Carrétéro, A. Barthélémy, P.

Appel, P. Maletinsky, J.-V. Kim, J. Y. Chauleau, N. Jaouen, M. Viret, M. Bibes, S. Fusil, V. Jacques, *Nature* **2017**, *549*, 252.

[48]   D. Kan, I. Takeuchi, *J. Appl. Phys.* **2010**, *108*, 014104.

[49]   F. Johann, A. Morelli, D. Biggemann, M. Arredondo, I. Vrejoiu, *Phys. Rev. B* **2011**, *84*, 094105.

[50]   H. Béa, M. Bibes, X.-H. Zhu, S. Fusil, K. Bouzehouane, S. Petit, J. Kreisel, A. Barthélémy, *Appl. Phys. Lett.* **2008**, *93*, 072901.

[51]   H. Béa, B. Dupé, S. Fusil, R. Mattana, E. Jacquet, B. Warot-Fonrose, F. Wilhelm, A. Rogalev, S. Petit, V. Cros, A. Anane, F. Petroff, K. Bouzehouane, G. Geneste, B. Dkhil, S. Lisenkov, I. Ponomareva, L. Bellaiche, M. Bibes, A. Barthélémy, *Phys. Rev. Lett.* **2009**, *102*, 217603.

[52]   J. Allibe, S. Fusil, K. Bouzehouane, C. Daumont, D. Sando, E. Jacquet, C. Deranlot, M. Bibes, A. Barthélémy, *Nano Lett.* **2012**, *12*, 1141.

[53]   D. Sando, A. Agbelele, D. Rahmedov, J. Liu, P. Rovillain, C. Toulouse, I. C. Infante, A. P. Pyatakov, S. Fusil, E. Jacquet, C. Carrétéro, C. Deranlot, S. Lisenkov, D. Wang, J.-M. M. Le Breton, M. Cazayous, A. Sacuto, J. Juraszek, A. K. Zvezdin, L. Bellaiche, B. Dkhil, A. Barthélémy, M. Bibes, *Nat. Mater.* **2013**, *12*, 641.

[54]   G. Radtke, C. Maunders, A. Saúl, S. Lazar, H. J. Whitfield, J. Etheridge, G. A. Botton, *Phys. Rev. B* **2010**, *81*, 85112.

[55]   H. Kurata, S. Isojima, M. Kawai, Y. Shimakawa, S. Isoda, *J. Microsc.* **2009**, *236*, 128.

[56]   M. Bugnet, G. Radtke, G. A. Botton, *Phys. Rev. B* **2013**, *88*, 201107.

[57]   K.-T. Ko, M. H. Jung, Q. He, J. H. Lee, C. S. Woo, K. Chu, J. Seidel, B.-G. Jeon, Y. S. Oh, K. H. Kim, W.-I. Liang, H.-J. Chen, Y.-H. Chu, Y. H. Jeong, R. Ramesh, J.-H. Park, C.-H. Yang, *Nat. Commun.* **2011**, *2*, 567.

[58]   M. D. Rossell, R. Erni, M. P. Prange, J.-C. Idrobo, W. Luo, R. J. Zeches, S. T. Pantelides, R. Ramesh, *Phys. Rev. Lett.* **2012**, *108*, 047601.

[59]   Y. Nahas, S. Prokhorenko, J. Fischer, B. Xu, C. Carrétéro, S. Prosandeev, M. Bibes, S. Fusil, B. Dkhil, V. Garcia, L. Bellaiche, *Nature* **2020**, *577*, 47.

[60]   W. Ratcliff, D. Kan, W. Chen, S. Watson, S. Chi, R. Erwin, G. J. McIntyre, S. C. Capelli, I. Takeuchi, *Adv. Funct. Mater.* **2011**, *21*, 1567.

[61]   A. Agbelele, D. Sando, C. Toulouse, C. Paillard, R. D. Johnson, R. Rüffer, A. F. Popkov, C. Carrétéro, P. Rovillain, J.-M. Le Breton, B. Dkhil, M. Cazayous, Y. Gallais, M.-A. Méasson, A. Sacuto, P. Manuel, A. K.

Zvezdin, A. Barthélémy, J. Juraszek, M. Bibes, *Adv. Mater.* **2017**, *29*.

[62] A. Zalesskii, A. Zvezdin, A. Frolov, A. Bush, *J. Exp. Theor. Phys. Lett.* **2000**, *71*, 682.

[63] A. Agbelele, D. Sando, I. C. Infante, C. Carrétéro, S. Jouen, J. M. Le Breton, A. Barthélémy, B. Dkhil, M. Bibes, J. Juraszek, *Appl. Phys. Lett.* **2016**, *109*, 042902.

[64] D. Sando, F. Appert, S. R. Burns, Q. Zhang, Y. Gallais, A. Sacuto, M. Cazayous, V. Garcia, S. Fusil, C. Carrétéro, J. M. Le Breton, A. Barthélémy, M. Bibes, J. Juraszek, V. Nagarajan, *Phys. Rev. Mater.* **2019**, *3*, 104404.

[65] D. Lebeugle, D. Colson, A. Forget, M. Viret, P. Bonville, J. F. Marucco, S. Fusil, *Phys. Rev. B* **2007**, *76*, 024116.

[66] W. Saenrang, B. A. Davidson, F. Maccherozzi, J. P. Podkaminer, J. Irwin, R. D. Johnson, J. W. Freeland, J. Íñiguez, J. L. Schad, K. Reierson, J. C. Frederick, C. A. F. Vaz, L. Howald, T. H. Kim, S. Ryu, M. Veenendaal, P. G. Radaelli, S. S. Dhesi, M. S. Rzchowski, C. B. Eom, *Nat. Commun.* **2017**, *8*, 1583.

[67] A. M. Kadomtseva, Y. F. Popov, A. P. Pyatakov, G. P. Vorob'ev, A. K. Zvezdin, D. Viehland, *Phase Transitions* **2006**, *79*, 1019.

[68] H. Béa, M. Bibes, A. Barthélémy, K. Bouzehouane, E. Jacquet, A. Khodan, J.-P. Contour, S. Fusil, F. Wyczisk, A. Forget, D. Lebeugle, D. Colson, M. Viret, *Appl. Phys. Lett.* **2005**, *87*, 072508.

[69] D. Sando, T. Young, R. Bulanadi, X. Cheng, Y. Zhou, M. Weyland, P. Munroe, V. Nagarajan, *Jpn. J. Appl. Phys.* **2018**, *57*, 0902B2.

[70] J. Juraszek, O. Zivotsky, H. Chiron, C. Vaudolon, J. Teillet, *Rev. Sci. Instrum.* **2009**, *80*, 043905.